

The clustering amplitude of X-ray selected AGN at $z \sim 0.8$: evidence for a negative dependence on accretion luminosity

G. Mountrichas¹, A. Georgakakis^{2,1}, M.-L. Menzel², N. Fanidakis³, A. Merloni², Z. Liu^{2,4}, M. Salvato², K. Nandra²

¹*National Observatory of Athens, V. Paulou & I. Metaxa, 11532, Greece*

²*Max Planck Institut für Extraterrestrische Physik, Giessenbachstraße, 85748 Garching, Germany*

³*Max Planck Institut für Astronomie, Königstuhl, 17 D-69117, Heidelberg, Germany*

⁴*National Astronomical Observatories, Chinese Academy of Sciences, Beijing 100012, People's Republic of China.*

8 February 2016

ABSTRACT

The northern tile of the wide-area and shallow XMM-XXL X-ray survey field is used to estimate the average dark matter halo mass of relatively luminous X-ray selected AGN [$\log L_X(2 - 10 \text{ keV}) = 43.6^{+0.4}_{-0.4} \text{ erg/s}$] in the redshift interval $z = 0.5 - 1.2$. Spectroscopic follow-up observations of X-ray sources in the XMM-XXL field by the Sloan telescope are combined with the VIPERS spectroscopic galaxy survey to determine the cross-correlation signal between X-ray selected AGN (total of 318) and galaxies (about 20,000). We model the large scales (2–25 Mpc) of the correlation function to infer a mean dark matter halo mass of $\log M/(M_\odot h^{-1}) = 12.50^{+0.22}_{-0.30}$ for the X-ray selected AGN sample. This measurement is about 0.5 dex lower compared to estimates in the literature of the mean dark matter halo masses of moderate luminosity X-ray AGN [$L_X(2 - 10 \text{ keV}) \approx 10^{42} - 10^{43} \text{ erg/s}$] at similar redshifts. Our analysis also links the mean clustering properties of moderate luminosity AGN with those of powerful UV/optically selected QSOs, which are typically found in halos with masses few times $10^{12} M_\odot$. There is therefore evidence for a negative luminosity dependence of the AGN clustering. This is consistent with suggestions that AGN have a broad dark matter halo mass distribution with a high mass tail that becomes sub-dominant at high accretion luminosities. We further show that our results are in qualitative agreement with semi-analytic models of galaxy and AGN evolution, which attribute the wide range of dark matter halo masses among the AGN population to different triggering mechanisms and/or black hole fueling modes.

Key words: galaxies: active, galaxies: haloes, galaxies: Seyfert, quasars: general, black hole physics

1 INTRODUCTION

The study of the large scale clustering of Active Galactic Nuclei (AGN) links accretion events onto Supermassive Black Holes (SMBHs) with their environments and provides useful constraints on the conditions under which such events occur in the Universe. Different clustering properties are predicted for the AGN depending, among others, on the mechanism that triggers the accretion onto the SMBH (secular evolution vs mergers, Hopkins et al. 2008; Bonoli et al. 2009; Bournaud et al. 2011), the origin of the accreted material (e.g. stellar winds, Ciotti & Ostriker 2007; hot atmosphere, Croton et al. 2006; galactic disk, Fanidakis et al. 2011), assumptions on the AGN light-curve (e.g. Kauffmann & Haehnelt 2002; Wyithe & Loeb 2003; Hopkins et al. 2007), the significance of

AGN feedback processes (e.g. Thacker et al. 2009; Fanidakis et al. 2013b).

The different model assumptions above can be tested by estimating the clustering of AGN populations as a function of redshift and/or physical AGN parameters, such as accretion luminosity, Eddington ratio or black-hole mass. UV/optically selected broad-line QSOs for example, are shown to live in Dark Matter Haloes (DMH) with masses few times $10^{12} h^{-1} M_\odot$ independent of redshift and with a weak, if any, accretion-luminosity dependence (e.g. Croom et al. 2005; Myers et al. 2007; da Ângela et al. 2008; Ross et al. 2009; Shen et al. 2009, 2013). These results have been interpreted in the context of major-merger scenarios for the triggering of the accretion onto the SMBH (e.g. Hopkins et al. 2007). The weak luminosity dependence of the QSO clustering also argues against a tight relation between instantaneous accretion luminosity and black-hole

or DMH mass and has implications for the form of the accretion light curve (e.g. Hopkins et al. 2007; Lidz et al. 2006).

Despite the significance of these results it is recognised that powerful UV/optically bright QSOs represent a small fraction of the AGN population and are biased against even moderately obscured sources. It is therefore necessary to complement the results above with clustering investigations of AGN samples selected by alternative means. X-ray wavelengths are advantageous in that respect (e.g. Brandt & Alexander 2015). X-ray photons, especially at energies above the keV level, are least affected by obscuring dust and gas clouds along the line of sight. Also, the X-ray emission associated with stellar processes is typically orders of magnitude fainter than the AGN radiative output and therefore dilution effects by the host galaxy are negligible at X-rays even for low accretion luminosities. X-ray surveys therefore provide least biased AGN samples over a wide accretion luminosity baseline.

Clustering studies of moderate luminosity X-ray selected AGN typically measure mean dark matter halo masses of $\approx 10^{13} h^{-1} M_{\odot}$, at least to $z \approx 1.5$ (e.g. Coil et al. 2009; Krumpke et al. 2010; Allevato et al. 2011; Mountrichas & Georgakakis 2012; Mountrichas et al. 2013). When compared to UV/optically selected powerful QSOs, this result suggests a negative luminosity dependence of the AGN clustering, i.e. decreasing mean dark matter halo mass with increasing accretion luminosity. Possible interpretations include different AGN triggering mechanisms (e.g. Allevato et al. 2011), or diverse accretion modes (e.g. Fanidakis et al. 2013b) that dominate at different AGN luminosity regimes. There are also attempts to explore the luminosity dependence of the clustering using X-ray selected AGN only. These however, are met with moderate success. There are claims for a positive correlation between X-ray luminosity and clustering but the statistical significance of those results is small (e.g. Krumpke et al. 2012; Koutoulidis et al. 2013). A serious limitation is that current X-ray AGN samples are typically small in size. Statistical uncertainties therefore dominate and do not allow clustering investigations over a sufficiently large luminosity baseline. This issue can be addressed by combining clustering constraints from X-ray samples with different depths and survey areas that probe different parts of the luminosity function at a given redshift. There are currently numerous X-ray surveys with sizes typically $\lesssim 2 \text{ deg}^2$ that provide constraints on the statistical properties of moderate and low luminosity AGN. In contrast, the number of wide-area X-ray samples that provide sufficient statistics at the bright-end of the X-ray luminosity function is still limited.

One of the widest contiguous X-ray surveys that has recently been completed is the XMM-XXL (PI: Pierre). With a total area of 50 deg^2 on the sky split into two equally-sized sub-regions, the XMM-XXL is 1-2 dex larger in size compared to any current pencil-beam and deep survey used for clustering investigations. It therefore provides a unique resource for studying the population properties of X-ray AGN that are underrepresented in current small-area X-ray samples. In this paper we focus the clustering analysis to the equatorial sub-region of the XMM-XXL field, which benefits from extensive follow-up spectroscopy of X-ray sources as part of the SDSS-III (Eisenstein et al. 2011) BOSS (Baryon Oscillation Spectroscopic Survey; Dawson et al. 2013) ancillary observations programme. An additional advantage of the equatorial XMM-XXL field is that it overlaps with the VIPERS (Vimos Public Extragalactic Survey; Guzzo et al. 2014) galaxy spectroscopic survey. This programme provides redshifts for about 20,000 galaxies in the interval $0.5 \lesssim z \lesssim 1.2$ within the XMM-XXL field. The Sloan and VIPERS spectroscopy are combined to determine the AGN/galaxy cross-correlation function and then infer the bias

and dark matter halo mass of relatively luminous X-ray AGN [$\log L_X(2 - 10 \text{ keV}) = 43.6^{+0.4}_{-0.4} \text{ erg/s}$]. This approach is advantageous for clustering measurements of sparse samples, such as AGN, because the statistical errors are smaller compared to the auto-correlation function. We adopt $\Omega_m = 0.3$, $\Omega_{\Lambda} = 0.7$ and $\sigma_8 = 0.8$. For the clustering analysis the Hubble constant is set to $H_0 = 100 \text{ km s}^{-1} \text{ Mpc}^{-1}$ and all relevant quantities, such as halo masses, are parametrised by $h = H_0/100$. In the calculation of the X-ray luminosities we fix $H_0 = 70 \text{ km s}^{-1} \text{ Mpc}^{-1}$ (i.e. $h = 0.7$). This is to allow comparison with previous studies that also follow similar conventions.

2 THE DATA

2.1 Optically selected galaxy sample

The galaxy spectroscopic sample is from the VIPERS survey (Guzzo et al. 2014; Garilli et al. 2014). In brief the VIPERS programme uses the VIMOS (VIsible MultiObject Spectrograph, Le Fèvre et al. 2003) to perform deep optical spectroscopy over 24 deg^2 split between the W1 and W4 wide tiles of the Canada-France-Hawaii Telescope Legacy Survey. Potential targets for follow-up spectroscopy are selected to the magnitude limit $i'_{AB} = 22.5$ from the T0006 data release of the CFHTLS photometric catalogues¹. The science motivation of the VIPERS is the study of the large-scale structure of the Universe and the measurement of cosmological parameters at redshifts $z \approx 1$. An optical photometric colour pre-selection is therefore applied [$(r - i) > 0.5(u - g)$ or $(r - i) > 0.7$] to exclude low redshift galaxies from the target sample and maximise the number of spectroscopic identifications in the redshift interval $z = 0.5 - 1.2$. The first public data release (PDR-1) of the VIPERS programme includes a total of 62,862 spectra observed by the VIMOS instrument in both the W1 and W2 fields (Garilli et al. 2014). Each spectrum is assigned a quality flag that quantifies the reliability of the measured redshift. The analysis presented in this paper uses only the CFHTLS-W1 VIPERS field, which has X-ray coverage from the XMM-XXL survey (see below). We select only galaxies with flags 2 to 9 inclusive. This yields a sample of 20,109 galaxies in the redshift range $0.5 < z < 1.2$.

The VIPERS observations strategy is to cover the survey area with only one pass to maximise the volume probed. This approach however, imprints a characteristic cross shape on the survey footprint (see Fig. 1) as a result of the VIMOS field-of-view that is composed of four CCDs with gaps among them. This pattern should be accounted for in large scale clustering investigations. Additionally, the maximum number of science slits on VIMOS and the surface density of the targeted population result in a slit assignment efficiency of about 45% on the average, but variable across the survey area. Weather and night-sky conditions during the observations also affect the quality of the spectra and therefore the success rate of measuring reliable redshifts across the survey area. The above selection and instrumental effects are accounted for, following the

¹ Based on observations obtained with MegaPrime/MegaCam, a joint project of CFHT and CEA/DAPNIA, at the Canada-France-Hawaii Telescope (CFHT) which is operated by the National Research Council (NRC) of Canada, the Institut National des Sciences de l'Univers of the Centre National de la Recherche Scientifique (CNRS) of France, and the University of Hawaii. This work is based in part on data products produced at TERAPIX and the Canadian Astronomy Data Centre as part of the Canada-France-Hawaii Telescope Legacy Survey, a collaborative project of NRC and CNRS.

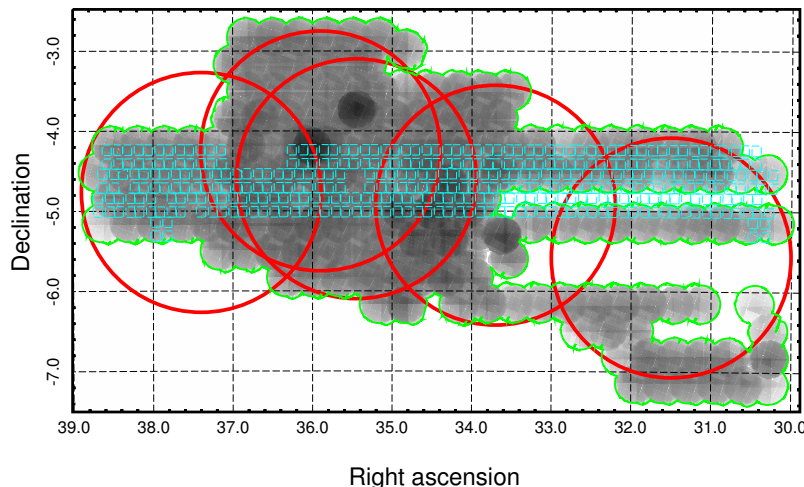


Figure 1. Layout of the XMM observations in the equatorial XMM-XXL field used in this paper. The distribution on sky coordinates of the EPIC PN+MOS exposure maps of individual XMM pointings is shown. The shading corresponds to different exposure times, with white being zero. The green line demarcates the limits of the area covered by the XMM data observed prior to 23 January 2012. XMM-XXL pointings observed after this date (total area of about 5 deg^2) are not included in the analysis. This incompleteness in the X-ray data coverage is manifested by the white (unexposed) horizontal stripes at e.g. $\delta \approx -5.5 \text{ deg}$ and $\alpha < 33.5 \text{ deg}$. The red circles mark the positions of the five SDSS-III special spectroscopic plates used to target X-ray sources in the field. The size of each circle is 3 deg in diameter, the field-of-view of the SDSS spectroscopic plates. The small cyan squares mark the positions of the VIMOS field-of-view quadrants of the VIPERS DRI.

methods described in de la Torre et al. (2013). The fraction of targets which have a measured spectrum is defined as the Target Sampling Rate (TSR) and the fraction of observed spectra with reliable redshift measurement as the Spectroscopic Sampling Rate (SSR). The latter is determined empirically as the ratio between the number of reliable redshifts and the total number of observed spectra. These two factors correct for incompleteness at large scales and are taken into account in form of weights applied to individual sources when measuring the galaxy auto-correlation function or the AGN/galaxy cross-correlation function. Incompleteness at small scales is also important. This is because of missing small-scale angular pairs due to the slit collisions and the finite number of VIMOS slits. This can be corrected for by comparing the angular auto-correlation function of the target and spectroscopic samples (de la Torre et al. 2013).

For the correlation measurements, we also generate a random catalogue that consists of $\approx 20\times$ the number of galaxies. The random catalogue is passed through both the photometric mask (i.e. bright stars) and the spectroscopic mask (Field-of-View of the spectrograph), so the random points have the same sky footprint as the real data. To test if the random sample is large enough to minimise the shot noise contribution to the estimated correlation functions, a catalogue with $100\times$ more random points than galaxies was also created. In the scales of interest for our analysis, i.e. $2\text{--}25 \text{ h}^{-1} \text{ Mpc}$, the estimated errors were similar in both cases. For computation efficiency we choose to use the random catalogue with 20 times as many points as real data.

2.2 AGN sample

The X-ray selected AGN sample is compiled from the XMM-XXL survey (PI: Pierre), which covers a total of about 50 deg^2 split

into two nearly equal area fields. The equatorial subregion of the XMM-XXL overlaps with the Canada-France-Hawaii Legacy Survey (CFHTLS) W1 field and extends to about 25 deg^2 the area covered by the original 11 deg^2 XMM-LSS survey (Clerc et al. 2014). The X-ray survey layout is presented in Fig. 1.

The reduction of the XMM observations, the construction of the source catalogue and the identification of the X-ray sources with optical counterparts follows the steps described in Georgakakis & Nandra (2011). Specific details on the analysis of the XMM-XXL survey data are presented by Liu et al. (2015, in prep.). In brief, the X-ray data reduction is carried out using the XMM Science Analysis System (SAS) version 12. XMM-XXL data observed prior to 23 January 2012 are analysed. At that date the XMM-XXL programme was partially complete. As a result the final catalogue of the equatorial XMM-XXL field presented in this paper is missing about 5 deg^2 worth of X-ray data. This incomplete data coverage is manifested by the white stripes in Fig. 1. The EPCHAIN and EMCHAIN tasks of SAS are employed to produce event files for the EPIC (European Photon Imaging Camera; Strüder et al. 2001; Turner et al. 2001) PN and MOS detectors respectively. Periods of elevated background because of flares are identified and excluded using a methodology similar to that described by Nandra et al. (2007). Sources are detected independently in five energy bands ($0.5\text{--}8$, $0.5\text{--}2$, $2\text{--}8$, $5\text{--}8$ and $7.5\text{--}12 \text{ keV}$) by applying a Poisson false detection probability threshold of $P < 4 \times 10^{-6}$. Systematic errors in the astrometric positions of the X-ray sources are corrected for using the EPOSCORR task of SAS and adopting as reference the SDSS (Sloan Digital Sky Survey; Gunn et al. 2006) DR8 catalogue (Aihara et al. 2011). Source fluxes are estimated by assuming a power-law X-ray spectrum with $\Gamma = 1.4$, i.e. similar to the diffuse X-ray Background, absorbed by the appropriate Galactic hydrogen column density derived from the HI map of Kalberla et al. (2005). The energy to flux conversion factors are such that

the counts from the 0.5–2, 0.5–8, 2–8, 5–8 and 7.5–12 keV bands are transformed to fluxes in the 0.5–2, 0.5–10, 2–10, 5–10 and 7.5–12 keV bands respectively. The final catalogue consists of 8,445 unique sources detected in at least one of the above spectral bands over a total area of about 20 deg^2 . These X-ray sources are matched to the SDSS-DR8 photometric catalogue (Aihara et al. 2011) using the Maximum-Likelihood method (Sutherland 1992). We assign secure counterparts to sources with Likelihood Ratio $LR > 1.5$. At that cut the spurious identification rate is about 6% and the total number of optical counterparts is 4,076.

Spectroscopic redshifts are mainly from the SDSS (Eisenstein et al. 2011; Smee et al. 2013). In addition to redshift measurements obtained as part of the SDSS-III’s Baryon Oscillation Spectroscopic Survey (BOSS; Dawson et al. 2013) programme, the equatorial region of the XMM-XXL field was also targeted by five special SDSS plates dedicated to follow-up spectroscopy of X-ray sources as part of the Ancillary Programs of SDSS-III. The distribution of these five plates within the equatorial XMM-XXL field is shown in Fig. 1. Targets were selected to have $f_X(0.5–10 \text{ keV}) > 10^{-14} \text{ erg s}^{-1} \text{ cm}^{-2}$ and $15 < r < 22.5$, where r is either the PSF magnitude in the case of optical unresolved sources (SDSS type=6) or the model magnitude for resolved sources. Specific details on these spectroscopic observations, including spectral classification and redshift quality flags based in visual classification are presented by Menzel et al. (2015, in prep). These spectroscopic data are complemented by additional redshift measurements from the Stalin et al. (2010) catalogue and the VIPERS Data Release 1 (Guzzo et al. 2014; Garilli et al. 2014) spectroscopic catalogue. In total 2816 X-ray sources are assigned redshifts and 813 of these are within the VIPERS mask. The redshift distribution of the latter sample is presented in Figure 2. In this paper we limit the clustering analysis to X-ray sources in the redshift interval $0.5 < z < 1.2$. This is to allow cross-correlation with the VIPERS galaxy sample. X-ray luminosities are estimated in the 2–10 keV band assuming a power-law X-ray spectrum with $\Gamma = 1.4$ for the k-corrections. The X-ray luminosity distribution of the $0.5 < z < 1.2$ sample is presented in Fig. 3. The median is $\log L_X(2–10 \text{ keV}) = 43.6^{+0.4}_{-0.4} \text{ erg s}^{-1}$. The errors correspond to the 16th and 84th percentiles around the median.

3 METHODOLOGY AND RESULTS

In this paper we infer the large scale bias of X-ray selected AGN using the 2-point correlation function. The Halo Occupation Distribution model (HOD, e.g. Peacock & Smith 2000; Berlind & Weinberg 2002) is often used to interpret the 2-point correlation functions of extragalactic sources and infer their large scale bias as well as their distribution in dark matter halos (e.g. Padmanabhan et al. 2009; de la Torre et al. 2013; Richardson et al. 2013). In this framework, the correlation function at small scales (typically $\lesssim 1–2 \text{ Mpc}$) is parametrised by the 1-halo term of the HOD, i.e. pairs of objects that live in the same halo, whereas the 2-halo term, i.e. pairs of objects that reside in different halos, models the correlation function at large scales ($\gtrsim 2 \text{ Mpc}$). Accurate measurements of the correlation function at small scales are essential to properly model the 1-halo term of the HOD and determine the distribution of AGN in dark matter halos. This measurement is challenging however, particularly in the case of the auto-correlation function of X-ray selected AGN. This is because of the sparsity of AGN samples and the typically small size of present-day X-ray surveys, which translate to small count statistics. One can overcome this limitation by

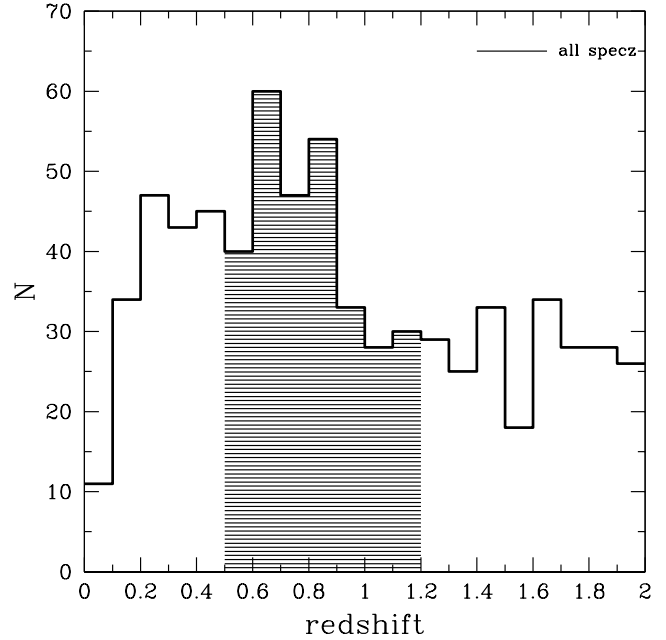


Figure 2. The solid histogram shows the redshift distribution of the 813 X-ray sources with secure redshifts that lie within the VIPERS spatial mask. The shaded region corresponds to the 318 X-ray sources in the redshift interval $0.5 < z < 1.2$ that are used in the clustering analysis presented in this paper.

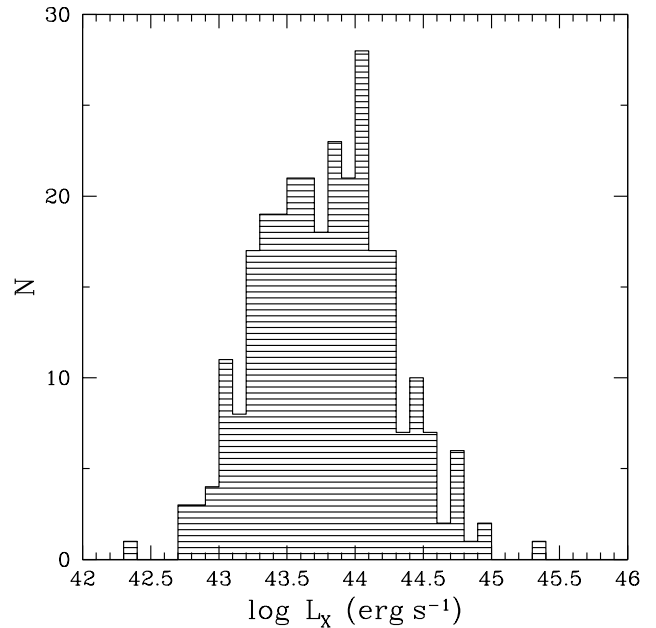


Figure 3. The X-ray luminosity distribution of the X-ray selected AGN sample in the redshift interval $0.5 < z < 1.2$ that is used in the clustering analysis presented in this paper. The median luminosity of the sample is $\log L_X(2–10 \text{ keV}) = 43.6 \text{ erg s}^{-1}$.

taking advantage of the higher space density of galaxies to sample the cosmic web and then determine the distribution of AGN on it by measuring the AGN/galaxy cross-correlation function. Shot noise is suppressed when counting AGN/galaxy pairs and the impact of sample variance on the results can be better controlled. Nevertheless, using the HOD to model the AGN/galaxy cross-correlation function requires large samples of both AGN and galaxies with well controlled systematics. This approach is therefore still limited to few datasets (e.g. Miyaji et al. 2011; Krumpe et al. 2012; Richardson et al. 2013), while there are also concerns that the HOD parameterisation of AGN samples may suffer degeneracies that lead to ambiguities in the inferred distribution in dark matter halos (e.g. Shen et al. 2013).

In this paper we use only the linear regime of the dark matter power spectrum to infer the large scale bias of AGN and determine the mean dark matter halo of the population (e.g. Allevato et al. 2011, 2012, 2014). The following sections describe how the AGN/galaxy cross-correlation function and galaxy auto correlation functions are measured and how they are modelled to infer the clustering amplitude of X-ray selected AGN.

3.1 Spatial clustering measurements via 2-point correlation functions

The equations presented next, are valid for the estimation of both the autocorrelation and cross-correlation function. If an equation needs to be modified to be used for a cross-correlation measurement, then the modified version of the equation is also given. The distance r between two objects in real-space can be decomposed into separations along the line of sight, π , and perpendicular to the line of sight, σ . If s_1 and s_2 are the distances of two objects 1, 2, measured in redshift-space, and θ the angular separation between them, then σ and π are defined as

$$\pi = (s_2 - s_1), \text{ along the line-of-sight,} \quad (1)$$

$$\sigma = \frac{(s_2 + s_1)}{2} \theta, \text{ across the line-of-sight.} \quad (2)$$

The 2-parameter redshift-space correlation function is then estimated as

$$\xi(\sigma, \pi) = \frac{DD(\sigma, \pi)}{DR(\sigma, \pi)} - 1, \quad (3)$$

where $DD(\sigma, \pi)$ are the data-data pairs at separations σ, π . $DR(\sigma, \pi)$ are the AGN-random pairs (cross-correlation) or galaxy-random pairs (galaxy autocorrelation). This estimator has the advantage that requires a random catalogue that accounts only for the selection function of galaxies, which is typically a spatial filter. More advanced estimators, such as that of (Landy & Szalay 1993), require the construction of random catalogues for the X-ray sources as well. This might introduce systematic biases into the calculations since X-ray observations have variable sensitivity across the field of view, which is challenging to quantify accurately. In redshift-space the clustering is affected on small scales by the rms velocity dispersion of AGN along the line of sight and by dynamical infall of matter into higher density regions. To first order, only the radial component of $\xi(\sigma, \pi)$ is affected by redshift-space distortions. We can therefore remove this bias by integrating along the line of sight, π , to calculate the projected cross-correlated function, $w_p(\sigma)$:

$$w_p(\sigma) = 2 \int_0^\infty \xi(\sigma, \pi) d\pi. \quad (4)$$

The value of the upper limit of the integral in equation 4, π_{max} , has to be determined for the estimation of the galaxy autocorrelation and the AGN/galaxy cross-correlation functions. For that, the projected correlation function, $w_p(\sigma)$, is computed for different π_{max} values and the bias is then estimated for each measurement. Fig. 4 presents the bias results as a function of π_{max} . The clustering signal saturates for $\pi_{max} = 30$ Mpc and $\pi_{max} = 20$ Mpc, for the galaxy autocorrelation function (stars) and the AGN/galaxy cross-correlation function (circles), respectively. In each case, the signal is underestimated at smaller scales and at larger scales the noise from uncorrelated pairs is increased. Therefore, we adopt these two different π_{max} values for each correlation function in our analysis. The real-space correlation function is the Fourier Transform of the linear power spectrum, $P_{2h}(k)$, i.e.

$$\xi_{DM}^{2h}(r) = \frac{1}{2\pi^2} \int P^{2h}(k) \frac{\sin(kr)}{kr} k^2 dk, \quad (5)$$

where k is the wavelength of the Fourier Transform and r the distance in real-space. The 2-halo term of the power spectrum can be approximated by (Cooray & Sheth 2002)

$$P^{2h}(k) \approx b^2 P_{lin}(k). \quad (6)$$

Equivalently,

$$\xi^{2h}(r) = b^2 \xi_{DM}^{2h}(r), \quad (7)$$

or, in terms of the projected correlation function

$$w_p^{2h}(\sigma) = b^2 w_{DM}^{2h}(\sigma). \quad (8)$$

$w_p^{2h}(\sigma)$ is the projected correlation function of the extragalactic population under consideration and $w_{DM}^{2h}(\sigma)$ is the projected correlation function of dark matter. Equation 5 is estimated, following Hamana et al. (2002) and then the projected correlation function of dark matter is calculated using

$$w_{DM}^{2h}(\sigma) = 2 \int_\sigma^\infty \frac{r \xi_{DM}^{2h}(r) dr}{\sqrt{(r^2 - \sigma^2)}} \quad (9)$$

The best-fit bias in equation 8 is estimated by applying a χ^2 minimization, $\chi^2 = \Delta^T M_{cov}^{-1} \Delta$, where M_{cov}^{-1} is the inverse of the covariance matrix, that quantifies the degree of correlation between the different bins of $w_p(\sigma)$. Δ is defined as $w_{p,2h} - w_{p,model}$, where $w_{p,model} = b^2 w_{DM}^{2h}(\sigma)$. In the case of a galaxy autocorrelation measurement, in equation 6, $b = b_g$, i.e. the galaxy bias, whereas in the case of an AGN/galaxy cross-correlation, $b = b_{AG}$, i.e. the AGN/galaxy bias. The AGN bias can then be inferred via

$$b_{AGN} = \frac{b_{AG}^2}{b_g} \quad (10)$$

For the estimation of the DMHM we adopt the ellipsoidal model of Sheth et al. (2001) and the analytical approximations of Van den Bosch (2002), which assume that on large scales the halo mass is only dependent on bias.

The uncertainties of the projected auto-correlation and cross-correlation measurements are estimated using the Jackknife methodology (e.g. Ross et al. 2008). The area of the survey is split into $N_{JK} = 20$ sections and the correlation function is measured N_{JK} times by excluding one section each time. For comparison, bootstrap errors are also estimated by performing 100 resamplings with replacement (e.g. Loh 2008). Both the Jackknife and bootstrap resampling methods yield similar covariance matrices and hence, similar uncertainties for the inferred bias and the dark matter halo mass. The errors estimates presented in the rest of this paper are based on the Jackknife method.

3.2 Applying corrections for redshift incompleteness to the VIPERS galaxy sample

For the determination of the AGN/galaxy cross-correlation function and the galaxy auto-correlation function in the XMM-XXL field equation (3) has to be modified to account for the spectroscopic window function and the sampling rate of the VIPERS galaxy sample (see Section 2.1). Following the analysis of de la Torre et al. (2013) to account for the completeness variations from quadrant to quadrant (large-scale incompleteness), each galaxy pair is weighted by the inverse of the effective sampling rate in each quadrant Q

$$w(Q) = (SSR(Q) \times TSR(Q))^{-1}. \quad (11)$$

Incompleteness at small scales because of slit collisions or the finite number of science slits available (see Section 2.2) is corrected for by adopting the methodology of Hawkins et al. (2003). Each galaxy pair separated by angle θ is weighted up by the factor

$$\frac{1}{w^A(\theta)} = \frac{1 + w_s(\theta)}{1 + w_p(\theta)}. \quad (12)$$

$w_p(\theta)$ is the angular correlation function of the parent sample (potential targets) and $w_s(\theta)$ is the angular correlation function of those sources that have a measured spectrum (spectroscopic sample). The large-scale incompleteness is also included in these calculations, i.e. each galaxy pair is weighted by $w(Q)$. The small-scale incompleteness affects the measurements on scales smaller than $\theta = 0.03$ deg or $1 \text{ h}^{-1} \text{ Mpc}$ comoving at $z = 0.7$ (Fig. 5). This is smaller than the scales of interest for our analysis, $2 - 25 \text{ Mpc}$. Nevertheless, the effect has been taken into account in the clustering measurements. The total weight applied on each DD and DR pair is

$$D_G D_G(r) = \sum_{i=1}^{N_G} \sum_{j=i+1}^{N_G} w_i(Q_i) w_j(Q_j) w_{GG}^A(\theta_{ij}) \quad (13)$$

$$D_g R(r) = \sum_{i=1}^{N_g} \sum_{j=1}^{N_r} w_i(Q_i) \quad (14)$$

Same corrections are applied in the case of the AGN/galaxy cross-correlation measurements. Fig. 5 (triangles) shows the small-scales incompleteness effect, for this case. The total weight assigned in each AGN/galaxy pair is

$$D_A D_g(r) = \sum_{i=1}^{N_A} \sum_{j=1}^{N_g} w_j(Q_j) w_{AG}^A(\theta_{ij}) \quad (15)$$

3.3 Results

Figure 6 plots the projected auto-correlation function of the galaxy sample and the AGN/galaxy cross-correlation function. These are estimated from equations (3) and (4) after applying the spatially variable weights described in Section 3.2. We then use equation (8) in combination with the dark matter correlation function of Hamana et al. (2002) to model the measured correlation functions and estimate the bias of AGN. In this calculation we use spatial scales in the range $2 - 25 \text{ Mpc}$ to fit the correlation functions. The inferred bias is then converted to mean dark matter halo mass using the model by Sheth et al. (2001) as explained in Section 3.1.

For the galaxy sample we estimate $b = 1.22^{+0.03}_{-0.03}$ and a mean dark matter halo mass of $\log M/(M_\odot h^{-1}) = 12.28^{+0.05}_{-0.07}$. Within the uncertainties, this is in fair agreement with

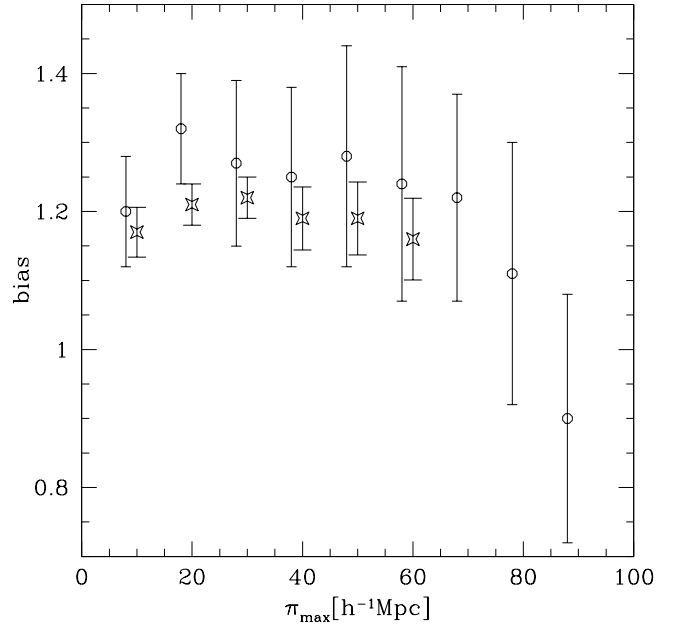


Figure 4. Bias estimations for the galaxy autocorrelation (stars) and the AGN/galaxy cross-correlation (circles) as a function of π_{max} . The clustering signal saturates for $\pi_{max} = 30 \text{ Mpc}$ and $\pi_{max} = 20 \text{ Mpc}$, for the galaxy autocorrelation function and the AGN/galaxy cross-correlation function, respectively. The circles are offset in the horizontal direction by -2 Mpc for clarity.

$\log M/(M_\odot h^{-1}) = 12.36^{+0.04}_{-0.05}$, determined by de la Torre et al. (2013) using both the W1 and W4 VIPERS fields.

The estimated bias and mean dark matter halo of AGN are presented in Table 1. We find that X-ray selected AGN in the XMM-XXL field are associated with halos of average mass $\log M/(M_\odot h^{-1}) = 12.50^{+0.22}_{-0.30}$. For the sake of reproducibility of these results the covariance matrices for both the galaxy auto-correlation and the AGN/galaxy cross-correlation functions are presented in Table 2.

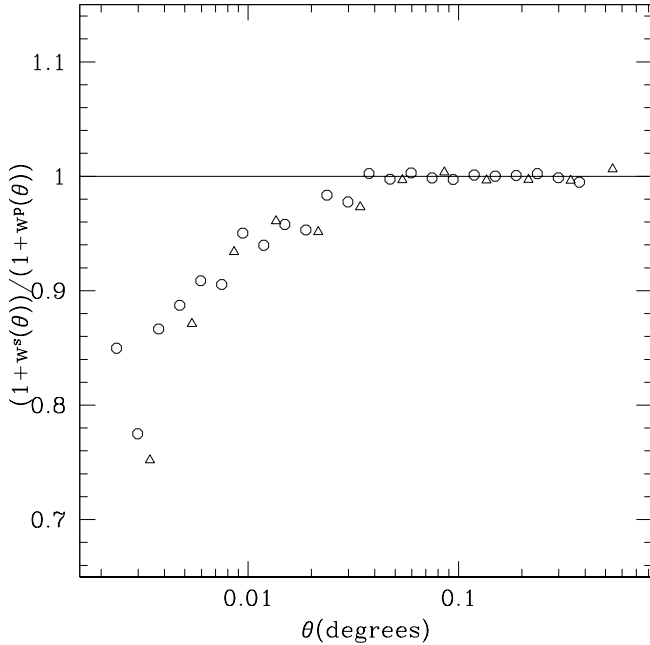
It has been shown (van den Bosch et al. 2013) that the integration of equation 4 to a finite π_{max} , rather than infinity, introduces systematic errors in the calculation of the projected correlation function and may lead to the underestimation of the inferred bias of extragalactic sources because of residual redshift distortions. We investigate the impact of this effect to the results by estimating the correction factors proposed by van den Bosch et al. (2013) and applying them on the galaxy auto-correlation function and the galaxy-AGN cross-correlation function. We use the linear power spectrum in real-space and redshift-space to estimate the correction factor, as described in equation (48) of van den Bosch et al. (2013) and then apply this correction function on the projected correlation function, following their equation (47). This approach yields an AGN bias of $1.53^{+0.20}_{-0.19}$, that corresponds to a halo with average mass $\log M/(M_\odot h^{-1}) = 12.63^{+0.23}_{-0.28}$. In the rest of the paper we use the values of bias and DMH mass listed in Table 1, i.e. not corrected for residual velocity distortions. This is because we are comparing our results to previous studies on the clustering of AGN that have ignored this effect.

Table 1. X-ray AGN and galaxy samples in the VIPERS field within the redshift range of $0.5 \leq z \leq 1.2$.

sample	No. of sources	$\langle z \rangle$	$\langle \log L_X \rangle$ (erg s^{-1})	b_{CCF}	b_{ACF}	$\log M_{DMH}$ ($h^{-1} M_\odot$)
AGN	318	0.81	43.6	$1.32^{+0.08}_{-0.08}$	$1.43^{+0.18}_{-0.18}$	$12.50^{+0.22}_{-0.30}$
galaxies	20,109	0.71			$1.22^{+0.03}_{-0.03}$	$12.28^{+0.05}_{-0.07}$

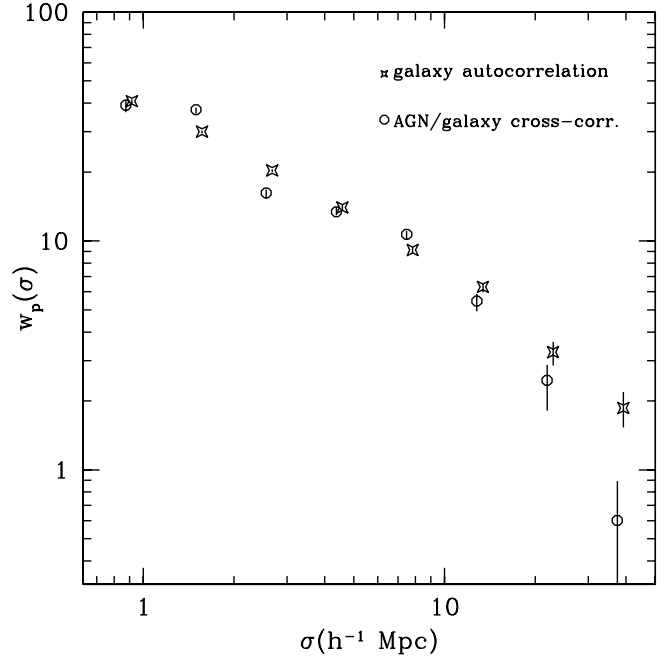
Table 2. The covariance matrices (not normalized) for the galaxy autocorrelation function and the AGN/galaxy cross-correlation function.

$\sigma(h^{-1} \text{ Mpc})$	galaxy autocorrelation					AGN/galaxy cross-correlation				
	2.68	4.58	7.84	13.41	23.94	2.68	4.58	7.84	13.41	23.94
2.68	2.801	1.783	1.944	1.581	0.784	8.667	1.925	0.072	2.053	0.8723
4.58		1.924	1.741	1.329	0.693		7.615	2.099	2.240	3.245
7.84			1.997	1.809	1.219			2.956	-0.341	0.742
13.41				2.139	1.855				3.922	2.496
23.94					2.217					4.939


Figure 5. The effect of small-scale incompleteness (see text). Circles present the angular pair completeness of the galaxy autocorrelation function and triangles the AGN/galaxy cross-correlation function, measured following Hawkins et al. (2003). The small-scale incompleteness affect the measurements on scales $\theta < 0.03$ deg. The large-scale incompleteness has also been taken into account.

4 DISCUSSION

We use the overlap between the XMM-XXL X-ray survey and the VIPERS optical spectroscopic sample in the CFHTLS-W1 field to estimate the cross-correlation function of relatively luminous [$L_X(2 - 10 \text{ keV}) \approx 10^{43.6} \text{ erg s}^{-1}$] X-ray selected AGN with


Figure 6. The projected galaxy autocorrelation function (stars) and the AGN/galaxy cross-correlation function (circles). The errors are the 16th and 84th percentiles of the distribution of $w_p(\sigma)$ from 20 Jackknife regions. The circles are offset in the horizontal direction by $\log = -0.02$ for clarity.

galaxies in the redshift interval $z = 0.5 - 1.2$. We infer a mean bias for the AGN $b = 1.43^{+0.18}_{-0.18}$ and an average DMH mass of $\log M/(M_\odot h^{-1}) = 12.50^{+0.22}_{-0.30}$.

A number of studies determine mean DMH masses for X-ray selected AGN at luminosities similar to those probed by the XMM-XXL sample presented in this paper. Krumpe et al. (2012) for ex-

ample, explore the clustering of AGN in the RASS (ROSAT All-Sky Survey; Voges et al. 1999). Their highest redshift sub-sample has $z = 0.36 - 0.50$ and a mean X-ray luminosity $\log L_X(2 - 10 \text{ keV}) \approx 43.8$ (units erg/s; see Fanidakis et al. (2013b) for the conversion of RASS band fluxes to 2-10 keV luminosities). For these sources they estimate a mean dark matter halo mass of $\log M/(M_\odot h^{-1}) = 12.51^{+0.28}_{-0.25}$. Starikova et al. (2011) measure the clustering of X-ray selected AGN in the Chandra Boötes field (Murray et al. 2005). Their sample with $z = 1.00 - 1.68$ has a mean X-ray luminosity $\log L_X(2 - 10 \text{ keV}) \approx 43.6$ (units erg/s). The inferred DMH mass is $\log M/(M_\odot h^{-1}) = 12.69 \pm 0.24$. Although the DMH masses determined in the above works are in broad agreement with our estimates, the different redshift intervals render the comparison hard to interpret. Additionally, Allevato et al. (2011) estimate dark matter halo masses for X-ray selected AGN in the XMM-COSMOS field (Hasinger et al. 2007) that are higher than the measurements above. For their subsample with median redshift $z = 1.3$ and median X-ray luminosity $\log L_X(2 - 10 \text{ keV}) \approx 44.0 \text{ erg s}^{-1}$ they determine $\log M/(M_\odot h^{-1}) = 13.12 \pm 0.12$. These higher dark matter halo mass measurements compared to our results and other previous studies at similar redshifts and luminosities may be related to sample variance effects. The COSMOS field is known to be rich in cosmic structures (Gilli et al. 2009; Skibba et al. 2015), which may bias clustering measurements. Our approach for inferring the clustering properties of AGN via the AGN/galaxy cross-correlation function should at least partly account for sample variance effects. Nevertheless, larger samples are needed to further explore this issue.

The X-ray AGN sample presented in this paper does not span a sufficiently large luminosity baseline to explore variations of the clustering amplitude with luminosity. We can nevertheless compare our results with previous studies on the clustering properties of moderate luminosity [$\log L_X(2 - 10 \text{ keV}) \lesssim 43.4 \text{ erg s}^{-1}$] X-ray selected AGN at redshifts similar to the sample presented in this paper (e.g. Coil et al. 2009; Gilli et al. 2009; Starikova et al. 2011; Allevato et al. 2012; Mountrichas et al. 2013). We restrict the comparison to those clustering studies that use redshift slices for the AGN samples that are relatively narrow and similar to ours ($0.5 < z < 1.2$). This is because of suggestions that the clustering strength of AGN may be a strong function of both redshift and accretion luminosity (Fanidakis et al. 2013b). The investigation of the luminosity dependence of the AGN clustering therefore requires samples that are selected at similar and relatively narrow redshift intervals.

Figure 7 plots DMH mass as a function of accretion luminosity and compares the mean DMH mass determined for the XMM-XXL AGN with previous estimates in the literature at lower luminosities. Moderate luminosity AGN in this figure are associated with mean DMH masses $\approx 10^{13} h^{-1} M_\odot$. These estimates are about 0.5 dex more massive than the mean DMH mass inferred for the XMM-XXL AGN sample. This is evidence for a negative luminosity dependence of the AGN clustering at $z \approx 0.8$, i.e. decreasing mean dark matter halo mass with increasing accretion luminosity. This trend is contrary to previous claims for a weak positive correlation between accretion luminosity and dark matter halo mass at $z \approx 1$ (e.g. Plionis et al. 2008; Krumpe et al. 2012; Koutoulidis et al. 2013). We attribute this apparent discrepancy to the different luminosity intervals of previous studies. Figure 7, combines clustering measurements from both deep small-area surveys and bright wide-area samples (XMM-XXL) and therefore covers a much wider luminosity baseline compared to any previous study at $z \approx 0.8$.

The XMM-XXL data point in Fig. 7 also links the relatively high clustering properties of moderate luminosity X-ray AGN (i.e. DMH masses $\approx 10^{13} h^{-1} M_\odot$) with those of powerful optical/UV selected QSOs, which typically reside in DMH of few times $10^{12} h^{-1} M_\odot$ (Croom et al. 2005; da Ângela et al. 2008; Ross et al. 2009). Variations of the clustering with accretion luminosity may indicate different AGN triggering mechanisms (e.g. Allevato et al. 2011; Mountrichas et al. 2013) and/or different black hole fuelling modes (e.g. Fanidakis et al. 2013a,b) as a function of AGN luminosity. The latter scenario is explored in Figure 7, which overplots the predictions of the GALFORM semi-analytic model (Bower et al. 2006; Fanidakis et al. 2012, 2013b) on the DMH mass vs $L_X(2 - 10 \text{ keV})$ plane. The GALFORM model postulates two modes for growing black holes. The first is associated with star-formation events (“starburst” mode). It assumes that a fraction of the cold gas in galaxies that is available for star-formation accretes onto the SMBH and it occurs when the host galaxy experiences a disk instability, or a major/minor merger in a gas rich disk. The second fuelling mode of GALFORM is decoupled from star-formation and takes place in quiescent galaxies (“hot-halo” mode). This is the case of DMHs with a diffuse hot gas component in quasi-hydrostatic equilibrium, which accretes onto the SMBH without being cooled first onto the galactic disk. By construction the two black hole fuelling modes in GALFORM operate in different large scale environments. Starburst AGN are typically found in relatively small DMHs, while hot-halo mode AGN also extend to very massive haloes (for more details see Fanidakis et al. 2013b). The interplay between the two modes produces the complex relation between accretion luminosity and mean DMH mass shown in Figure 7. At low and moderate luminosities both modes co-exist. There is therefore a wide distribution of DMH masses, including some massive ones associated with hot-halo mode AGN, which bias the average DMH mass of the population to high values. At high accretion luminosities however, the “hot-halo” mode becomes sub-dominant and the mean DMH mass of the population drops sharply to the typical DMH mass of the Starburst mode AGN. The observational constraints plotted in Figure 7, including the XMM-XXL data-point, also suggest an abrupt change in the mean dark matter halo mass of X-ray selected AGN, in qualitative agreement with the GALFORM predictions. At the same time however, the comparison of the observations with the GALFORM SAM predictions also reveals important differences. The transition luminosity, where the mean DMH mass of the AGN population shows a sudden drop, is brighter by about 0.5 dex in the model compared to the data. In GALFORM the accretion luminosity at which the starburst mode fueling becomes dominant over the hot-halo mode accretion (and therefore the mean clustering properties of the population change) is related to the adopted value for the viscosity ($\alpha = 0.087$ in GALFORM), the cooling properties of the parent DMH and the timescale that the cooled gas is accreted onto the central SMBH in the hot-halo accretion mode. Modifying these parameters could potentially improve the agreement between the observed clustering properties of X-ray AGN and the GALFORM predictions. Such modifications however, may also require retuning of other parameters of GALFORM.

Alternatively, the apparent discrepancy between the observational results and the GALFORM model predictions on the turnover luminosity in Figure 7 may indicate that physical processes other than hot gas accretion are responsible for low and moderate luminosity X-ray selected AGN at $z \approx 1$. Ciotti & Ostriker (2007) for example suggest that mass loss from evolved stars could provide a sufficient supply of gas to trigger recursive accretion events

onto supermassive black holes in early-type galaxies. Population studies at low redshift indeed suggest that this process may be responsible for the fuelling of low and moderate luminosity AGN in passive hosts (Kauffmann & Heckman 2009). These early-type galaxies are also expected to be associated on average with massive dark matter halos (e.g. Zehavi et al. 2011; Mostek et al. 2012), thereby increasing the mean bias of the AGN population at low and moderate accretion luminosities. Another possibility is that of gravitational interactions between galaxies or tidal disruption events in dense environments. These processes may also play an important role in fuelling AGN activity at low and moderate luminosities.

All the scenarios outlined above require a baseline black hole fuelling mode that operates in small dark matter halos and produces AGN over a wide luminosity baseline (including powerful ones) and an additional process that takes place in denser environments and produces low and moderate luminosity accretion events. In this picture it is variations in the width of dark matter halo mass distribution at a given accretion luminosity that produces the observed luminosity trend of the mean AGN dark matter halo mass in Figure 7.

The considerations above also highlight the importance of constraining the full distribution of AGN in DMHs, not just the mean, which is sensitive to the tails of a skewed distribution. Mountrichas et al. (2013) for example, find that the average dark matter halo mass of moderate luminosity X-ray selected AGN drops from $\log M/(M_\odot h^{-1}) \approx 13.0$ to $\log M/(M_\odot h^{-1}) \approx 12.5$ after removing only 5 per cent of the AGN population associated with X-ray selected groups. This suggests that most moderate luminosity X-ray AGN live in halos with masses few times $10^{12} h^{-1} M_\odot$. Leauthaud et al. (2015) assumed that AGN hosts follow the same stellar-to-halo mass relation as non-active galaxies (see also Georgakakis et al. 2014; Krumpel et al. 2015) and propose that the DMH distribution of moderate-luminosity X-ray AGN at $z < 1$ peaks at relatively low masses with a tail extending to group-size halos ($\approx 10^{13} h^{-1} M_\odot$). Constraints on the Halo Occupation Distribution of AGN are broadly consistent these findings (e.g. Miyaji et al. 2011; Allevato et al. 2012). The analysis presented in this paper, suggests that at high accretion luminosities [$L_X(2-10\text{ keV}) \approx 10^{43.6} \text{ erg s}^{-1}$], the high mass tail of the X-ray AGN DMH distribution is reduced and as a result the mean DMH mass is considerably lower than moderate luminosity AGN.

5 CONCLUSIONS

A clustering analysis is applied to relatively luminous [$\log L_X(2-10\text{ keV}) \approx 43.6 \text{ erg/s}$] X-ray AGN in the redshift interval $z = 0.5 - 1.2$ extracted from the $\sim 25 \text{ deg}^2$ of the XMM-XXL field. Only scales of the correlation function that include the linear regime of the power spectrum are modelled, to derive the AGN bias and DMHM of the host galaxies. The analysis reveals that these sources live in haloes of $\log M/(M_\odot h^{-1}) = 12.50^{+0.22}_{-0.30}$. This mass is lower than moderate luminosity X-ray AGN at similar redshifts ($\log M/(M_\odot h^{-1}) \approx 13$) and similar to UV/optical selected QSOs. This is evidence for a decreasing mean dark matter halo mass for AGN with increasing accretion luminosity. These results are consistent with suggestions that the dark matter halo mass distribution of AGN is broad and includes a massive-end tail, which skews measurements of the mean dark matter halo mass of AGN to high values. This tail appears to become sub-dominant with increasing accretion luminosity. We also discuss the results in the context of cosmological semi-analytic models in which the broad

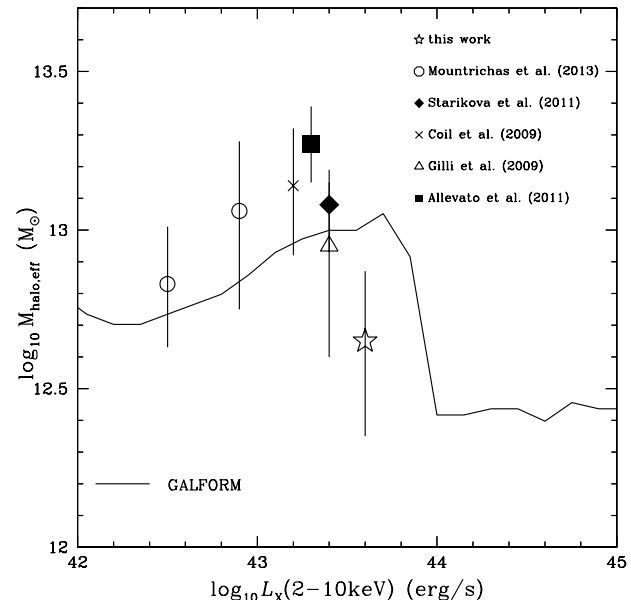


Figure 7. DMH mass as a function of accretion luminosity. Moderate luminosity AGN are associated with mean DMH masses of $\approx 10^{13} h^{-1} M_\odot$, i.e. about 0.5 dex more massive than the mean DMH mass inferred for the XMM-XXL AGN sample. Halo mass calculations are taken from Table 1 in Fanidakis et al. (2013) and have been converted to the same cosmology as the GALFORM model, i.e. $H_0 = 70 \text{ km s}^{-1} \text{ Mpc}^{-1}$. The solid line presents the complex relation between luminosity and halo mass, predicted by the GALFORM model. The predictions of the model at the $L_X > 10^{44} \text{ erg/s}$, corresponds to the clustering level of the starburst mode. This mode has only a weak dependence on the X-ray luminosity and therefore can be extrapolated to fainter luminosities.

dark matter halo mass distributon of AGN is related to different fuelling modes of the central balck hole. We show that the observed negative accretion luminosity dependence of the X-ray AGN clustering is in qualitative agreement with such models.

6 ACKNOWLEDGMENTS

The authors are grateful to the anonymous referee for helpful comments and Takamitsu Miyaji for useful discussions. GM acknowledges financial support from the THALES project 383549 that is jointly funded by the European Union and the Greek Government in the framework of the programme “Education and lifelong learning”. This paper uses data from the VIMOS Public Extragalactic Redshift Survey (VIPERS). VIPERS has been performed using the ESO Very Large Telescope, under the “Large Programme” 182.A-0886. The participating institutions and funding agencies are listed at <http://vipers.inaf.it>. Funding for SDSS-III has been provided by the Alfred P. Sloan Foundation, the Participating Institutions, the National Science Foundation, and the U.S. Department of Energy Office of Science. The SDSS-III web site is <http://www.sdss3.org/>. SDSS-III is managed by the Astrophysical Research Consortium for the Participating Institutions of the SDSS-III Collaboration including the University of Arizona, the Brazilian Participation Group, Brookhaven National Laboratory, Carnegie Mellon University, University of Florida, the French Participation Group, the German Participation Group, Harvard University, the Instituto de As-

trofísica de Canarias, the Michigan State/Notre Dame/JINA Participation Group, Johns Hopkins University, Lawrence Berkeley National Laboratory, Max Planck Institute for Astrophysics, Max Planck Institute for Extraterrestrial Physics, New Mexico State University, New York University, Ohio State University, Pennsylvania State University, University of Portsmouth, Princeton University, the Spanish Participation Group, University of Tokyo, University of Utah, Vanderbilt University, University of Virginia, University of Washington, and Yale University.

REFERENCES

- Aihara H., et al., 2011, *ApJS*, 193, 29
 Allevato V., et al., 2011, *ApJ*, 736, 99
 —, 2012, *ApJ*, 758, 47
 —, 2014, *ApJ*, 796, 4
 Berlind A. A., Weinberg D. H., 2002, *ApJ*, 575, 587
 Bonoli S., Marulli F., Springel V., White S. D. M., Branchini E., Moscardini L., 2009, *MNRAS*, 396, 423
 Bournaud F., Dekel A., Teyssier R., Cacciato M., Daddi E., Juneau S., Shankar F., 2011, *ApJ*, 741, 33
 Bower R. G., Benson A. J., Malbon R., Helly J. C., Frenk C. S., Baugh C. M., Cole S., Lacey C. G., 2006, *MNRAS*, 370, 645
 Brandt W. N., Alexander D. M., 2015, *A&A Rev.*, 23, 1
 Ciotti L., Ostriker J. P., 2007, *ApJ*, 662, 110
 Clerc N., Adami C., Lieu M., Maughan B., Pacaud F., Pierre M., Sadibekova T., Smith G. P., Valageas P., Altieri B., Benoist C., Maurogordato S., Willis J. P., 2014, *MNRAS*, 444, 2723
 Coil A. L., et al., 2009, *ApJ*, 701, 1484
 Cooray A., Sheth R., 2002, *Physics Reports*, 372, 1
 Croom S. M., et al., 2005, *MNRAS*, 356, 415
 Croton D. J., et al., 2006, *MNRAS*, 365, 11
 da Ângela J., et al., 2008, *MNRAS*, 383, 565
 Dawson K. S., et al., 2013, *AJ*, 145, 10
 de la Torre S., et al., 2013, *A&A*, 557, 54
 Eisenstein D. J., et al., 2011, *AJ*, 142, 72
 Fanidakis N., Baugh C. M., Benson A. J., Bower R. G., Cole S., Done C., Frenk C. S., 2011, *MNRAS*, 410, 53
 Fanidakis N., Macciò A. V., Baugh C. M., Lacey C. G., Frenk C. S., 2013a, *MNRAS*, 436, 315
 Fanidakis N., et al., 2012, *MNRAS*, 419, 2797
 —, 2013b, *MNRAS*, 435, 679
 Garilli B., et al., 2014, *A&A*, 562, 23
 Georgakakis A., Nandra K., 2011, *ArXiv*: 1101.4943
 Georgakakis A., et al., 2014, *MNRAS*, 443, 3327
 Gilli R., et al., 2009, *A&A*, 494, 33
 Gunn J. E., et al., 2006, *AJ*, 131, 2332
 Guzzo L., et al., 2014, *A&A*, 566, 108
 Hamana T., Yoshida N., Suto Y., 2002, *ApJ*, 568, 455
 Hasinger G., et al., 2007, *ApJS*, 172, 29
 Hawkins E., et al., 2003, *MNRAS*, 346, 78
 Hopkins P. F., Hernquist L., Cox T. J., Keres D., 2008, *ApJS*, 175, 356
 Hopkins P. F., Lidz A., Hernquist L., Coil A. L., Myers A. D., Cox T. J., Spergel D. N., 2007, *ApJ*, 662, 110
 Kalberla P. M. W., Burton W. B., Hartmann D., Arnal E. M., Baja, 2005, *A&A*, 440, 775
 Kauffmann G., Haehnelt M. G., 2002, *MNRAS*, 332, 529
 Kauffmann G., Heckman T. M., 2009, *MNRAS*, 397, 135
 Koutoulidis L., Plionis M., Georgantopoulos I., Fanidakis N., 2013, *MNRAS*, 428, 1382
 Krumpe M., Miyaji T., Coil A. L., 2010, *ApJ*, 713, 558
 Krumpe M., Miyaji T., Coil A. L., Aceves H., 2012, *ApJ*, 746, 1
 Krumpe M., Miyaji T., Husemann B., Fanidakis N., Coil A. L., Aceves H., 2015, *ApJ*, 815, 21
 Landy S. D., Szalay A. S., 1993, *ApJ*, 412, 64
 Le Fèvre O., Saisse M., Mancini D., Brau-Nogue S., Caputi O., Castinel L., D’Odorico S., Garilli B., Kissler-Patig M., Lu-
 cuix C., Mancini G., Pauget A., Sciarretta G., Scodreggio M., Tresse L., Vettolani G., 2003, in *Society of Photo-Optical Instru-
 mentation Engineers (SPIE) Conference Series*, Vol. 4841, In-
 strument Design and Performance for Optical/Infrared Ground-
 based Telescopes, Iye M., Moorwood A. F. M., eds., pp. 1670–
 1681
 Leauthaud A., et al., 2015, *MNRAS*, 446, 1874
 Lidz A., Hopkins P. F., Cox T. J., Hernquist L., Robertson B., 2006, *ApJ*, 641, 41
 Loh J. M., 2008, *ApJ*, 681, 726
 Miyaji T., Krumpe M., Coil A. L., Aceves H., 2011, *ApJ*, 726, 83
 Mostek N., Coil A. L., Moustakas J., Salim S., Weiner B. J., 2012, *ApJ*, 746, 15
 Mountrichas G., Georgakakis A., 2012, *MNRAS*, 420, 514
 Mountrichas G., et al., 2013, *MNRAS*, 430, 661
 Murray S. S., et al., 2005, *ApJS*, 161, 1
 Myers A. D., Brunner R. J., Nichol R. C., Richards G. T., Schnei-
 der D. P., Bahcall N. A., 2007, *ApJ*, 658, 85
 Nandra K., et al., 2007, *ApJ*, 660, 11
 Padmanabhan N., White M., Norberg P. and Porciani C., 2009, *MNRAS*, 397, 1862
 Peacock J. A., Smith R. E., 2000, *MNRAS*, 318
 Plionis M., Rovilos M., Basilakos S., Georgantopoulos I., Bauer F., 2008, *ApJ*, 674, 5
 Richardson J., Chatterjee S., Zheng Z., Myers A. D., Hickox R., 2013, *ApJ*, 774
 Ross N. P., Shanks T., Cannon R. D., Wake D. A., Sharp R. G., Croom S. M., Peacock J. A., 2008, *MNRAS*, 387, 1323
 Ross N. P., et al., 2009, *ApJ*, 697, 1634
 Shen Y., et al., 2009, *ApJ*, 697, 1656
 —, 2013, *ApJ*, 778, 98
 Sheth R. K., Mo H. J., Tormen G., 2001, *MNRAS*, 323, 1
 Skibba R. A., et al., 2015, *ApJ*, 807, 152
 Smee S., et al., 2013, *AJ*, 146, 32
 Stalin C. S., Petitjean P., Srianand R., Fox A. J., Coppolani F., Schwobe A., 2010, *MNRAS*, 401, 294
 Starikova S., et al., 2011, *ApJ*, 741, 15
 Strüder L., et al., 2001, *A&A*, 365, 18
 Sutherland W. & Saunders W., 1992, *MNRAS*, 259, 413
 Thacker R. J., Scannapieco E., Couchman H. M. P., Richardson M., 2009, *ApJ*, 693
 Turner M. J. L., et al., 2001, *A&A*, 365, 27
 Van den Bosch F. C., 2002, *MNRAS*, 331, 98
 van den Bosch F. C., More S., Cacciato M., Mo H., Yang X., 2013, *MNRAS*, 430, 725
 Voges W., et al., 1999, *A&A*, 349, 389
 Wyithe J. S. B., Loeb A., 2003, *ApJ*, 595, 614
 Zehavi I., et al., 2011, *Apj*, 736, 30